Journal of Materials Chemistry A

ROYAL SOCIETY OF CHEMISTRY

PAPER

View Article Online
View Journal | View Issue

Cite this: J. Mater. Chem. A, 2023, 11, 12910

A 3D lithiophilic ZIF-8@RGO free-standing scaffold with dendrite-free behavior enabling high-performance Li metal batteries†

Qi Liu,[ab] Rilei Wang,[a] Zhenfang Liu,[a] Xianshu Wang,*[d] Cuiping Han,[c] Hongbo Liu*[a] and Baohua Li*[b]

Li metal is an attractive anode material for electrochemical energy storage. However, the growth of Li dendrites accompanied with infinity-dimension changes, which leads to decreased coulombic efficiency and Li utilization, has long hampered practical application in rechargeable Li-metal batteries. Herein, a 3D ZIF-8@RGO scaffold with in-situ-formed abundant N/Zn sites after a convenient carbonization strategy is successfully demonstrated as both current collector and host material for Li metal anodes. Preferential Li deposition is predominantly accommodated into the 3D matrix free of dendrites by the synergetic effect of lithiophilic N/Zn nucleation sites and free-standing RGO with outstanding conductive properties. Profiting from the selective deposition and stable encapsulation, Li/ZIF-8@RGO anodes with preloading 5 mA h cm^{-2} Li can run for 600 h without short circuit and deliver a promoted coulombic efficiency of ~98.48% over 350 cycles. Moreover, the ZIF-8@RGO-based full cells exhibit exceptional cycling stability and rate capability.

Received 30th November 2022
Accepted 30th January 2023

DOI: 10.1039/d2ta09316b

rsc.li/materials-a

Introduction

Lithium (Li) metal-based batteries have attracted a renewed interest to meet ever-growing demands for portable electronics and electric vehicles.[1–3] In particular, Li metal with ultrahigh theoretical specific capacity (~3680 mA h g^{-1}) and ultralow redox potential (−3.04 V *versus* standard hydrogen electrode) is regarded as the ultimate anode material.[4,5] Despite the appealing advantages, its practical applications are still plagued by serious issues,[6,7] especially in terms of dendrite growth[8] and large changes in dimension,[9] attributed to the uneven Li plating/stripping processes, thus giving rise to low coulombic efficiency[10] and unstable interfacial chemistry.[11] This leads to reduced Li utilization, shorted cell lifetime and enhanced safety hazards with highly flammable organic electrolytes.

In this regard, colossal efforts have been focused on tackling these crucial issues from different perspectives, such as optimizing electrolyte compositions,[12–15] constructing artificial interfacial layers,[16–20] and developing solid-state electrolytes.[21–24] Despite the progress in these strategies, an emphasis on suppressing dendrite growth and repeated volume changes is still not simultaneously achieved for the high utilization (>~90%) of Li metal to meet the target of ~500 W h kg^{-1} energy density, particularly at high rates.[25] Alternatively, based on Sand's model, developing a 3D host with large specific surface area and suitable voids is supposed to be an effective approach to reduce the local current density and then promote a uniform plating behaviour.[26,27] More impressively, diverse carbon-based hosts (*i.e.*, porous carbon nanofibers,[28,29] carbon cloth,[30] porous carbon,[31–33] graphene[34] or C@MoS_2 (ref. 35)) possess superior properties in comparison with 3D metal hosts, such as higher electronic conductivity, more stable framework texture as well as obvious lightweight superiority. Nevertheless, there is a problem to be urgently solved of the poor affinity among carbon-based hosts and metallic Li to achieve highly reversible capacity with areal capacities of >~5 mA h cm^{-2} of Li metal anodes.[36–38] Therefore, effective strategies (for example, suitable seeding sites to promote the nucleation process[39]) to concurrently achieve dendrite-free but selected deposition and significantly reversible capacity during a long cycling must be explored, to ensure the availability of safe rechargeable Li metal-based batteries with high energy density.

[a]College of Materials Science and Engineering, Hunan University, Changsha, 410082, Hunan, China. E-mail: hndxlhb@163.com

[b]Shenzhen Key Laboratory of Power Battery Safety, Shenzhen Geim Graphene Center, Tsinghua Shenzhen International Graduate School, Tsinghua University, Shenzhen, 518055, China. E-mail: libh@mail.sz.tsinghua.edu.cn

[c]Faculty of Materials Science and Engineering, Institute of Technology for Carbon Neutrality, Shenzhen Institute of Advanced Technology, Chinese Academy of Sciences (CAS), Shenzhen, Guangdong, 518055, China

[d]National and Local Joint Engineering Laboratory for Lithium-ion Batteries and Materials Preparation Technology, Key Laboratory of Advanced Battery Materials of Yunnan Province, Faculty of Metallurgical and Energy Engineering, Kunming University of Science and Technology, Kunming, 650093, People's Republic of China. E-mail: xswang2016@m.scnu.edu.cn

† Electronic supplementary information (ESI) available. See DOI: https://doi.org/10.1039/d2ta09316b

Here, a 3D lithiophilic reduced graphene oxide-based scaffold formulated with abundant N/Zn active sites (denoted as ZIF-8@RGO) with preloaded metallic Li is developed as a stable high-capacity Li metal anode (5 mA h cm^{-2}). As-prepared ZIF-8@RGO skeleton is made of a free-standing network of RGO with moderate specific surface area and high electronic conductivity. The in-situ-formed abundant N/Zn active sites from the thermally reduced MOF material (ZIF-8) are demonstrated to be a key factor, distinguished from other carbon-based 3D scaffolds, for dendrite-free Li-plating/stripping behaviours. These lithiophilic seeding sites deliver a significantly lowered nucleation overpotential and enhanced lithiophilic property, thus giving rise to the facilitated uniform nucleation of Li metal. Consequently, the electrochemical properties of ZIF-8@RGO-based Li metal anodes by preloading ~5 mA h cm^{-2} with electrochemical methods are therefore significantly improved, which can stably operate for 600 hours at 1 mA cm^{-2} and keep a high coulombic efficiency of ~98.48% over 350 cycles. Notably, full cells coupled with $LiFePO_4$ possess superior cycling stability and rate performance, indicating great potential of high utilization for Li metal in practical applications.

Results and discussion

Fabrication and characterization of ZIF-8@RGO

A free-standing ZIF-8@RGO scaffold was fabricated *via* a simple route illustrated in Fig. S1.† The initial ZIF-8@GO free-standing film was first synthesized through suction filtration and then freeze-dried with liquid nitrogen. After further carbonization up to 800 °C for 3 hours, a ZIF-8@RGO scaffold with abundant N/Zn active sites was directly obtained.[40–43] As illustrated in Scheme 1a, such a free-standing electrode with a combination of 3D conductive channels and uniformly distributed lithiophilic N/Zn sites enables spatially homogeneous Li nucleation, enhanced transfer kinetics, reduced interfacial resistance as well as alleviated volume expansion effect, giving rise to dendrite-free plating behavior and high utilization of Li capacity. In sharp contrast, a bare Cu foil exhibits a detrimental but continuous growth of dendritic Li due to the obvious local current density (Scheme 1b). Furthermore, the free-standing ZIF-8@RGO delivers lower gravimetric density than a bare Cu collector, availing high energy density of a Li/ZIF-8@RGO composite anode. As expected, the ZIF-8@RGO/Li-metal anode exhibits a promoted uniform lithium deposition and improved cycling stability with a high areal capacity (>5 mA h cm^{-2}).

The scanning electron microscopy (SEM) image and X-ray diffraction (XRD) pattern (identified peaks at 7.35, 10.40 and 12.75° indexed as ZIF-8 material; JCPDS: 00-062-1030 (ref. 44)) in Fig. 1a and b clearly presented that ZIF-8 nanoparticles with an average diameter of 20–30 nm were homogenously anchored on the surface of GO free-standing films. After carbonization, the free-standing ZIF-8@GO film of ~300 μm successfully converted into a darker ZIF-8@RGO film (inset optical image in Fig. 1c). Furthermore, fracture morphology from SEM and energy-dispersive X-ray spectroscopy (EDS) further indicated that C, O, N and Zn elements were evenly distributed throughout RGO films, which would be beneficial for homogenous Li ion flux distribution in the as-prepared ZIF-8@RGO scaffolds proved by previous findings.[45] In addition, we further investigated the content of Zn and N elements by X-ray photoelectron spectroscopy (XPS), shown Table S1.† Compared to pure RGO, 0.24 wt% of Zn was captured in the ZIF-8@RGO electrode with a slight increase in C and a slight decrease in N, attributed to the carbonization of ZIF-8 material. The high-resolution XPS spectrum in Fig. 1d indicated that the surface chemical states of ZIF-8@RGO contained pyridinic nitrogen, quaternary ammonium nitrogen and nitrogen oxide in N 1s,

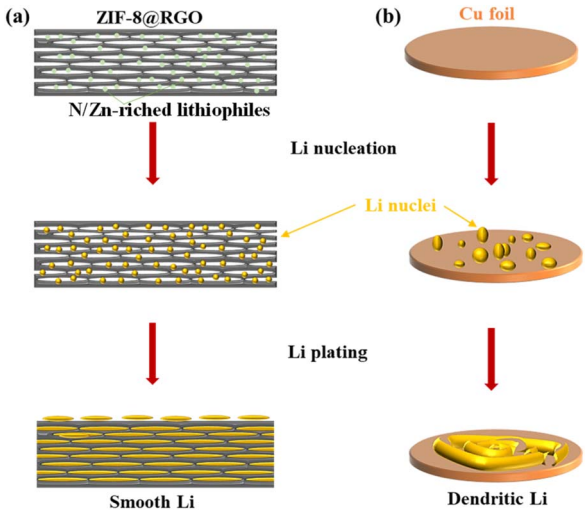

Scheme 1 Mechanism of the lithium nucleation of (a) ZIF-8@RGO and (b) bare Cu.

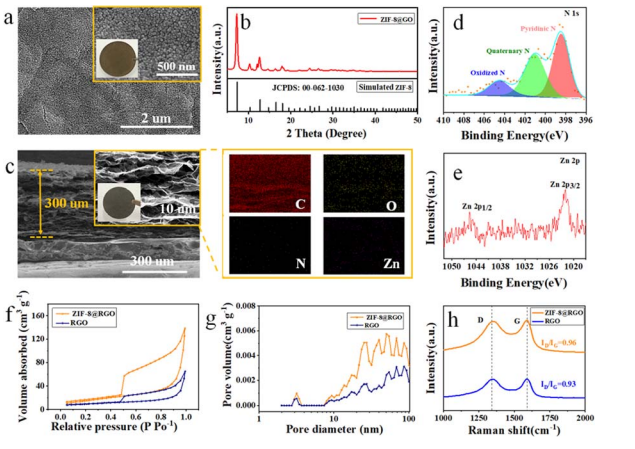

Fig. 1 Characteristics of ZIF-8@RGO. (a) SEM image of pure ZIF-8; insets: enlarged microstructure and optical image of ZIF-8@GO film. (b) XRD patterns of ZIF-8@GO. (c) Fracture morphology of SEM and corresponding EDS mapping for C, O, N, Zn elements of ZIF-8@RGO; inset: optical picture of the free-standing ZIF-8@RGO film. High-resolution XPS spectra of (d) N 1s and (e) Zn 2p of ZIF-8@RGO. (f) Nitrogen adsorption–desorption isotherms and (g) the corresponding pore size distributions calculated from the non-local density functional theory model. (h) Raman spectra of RGO and ZIF-8@RGO.

appearing at ~398.4 eV, ~401.1 eV and ~404.53 eV, respectively, inducing the uniform deposition of Li^+ with reduced nucleation overpotential during the plating. More importantly, the peaks at ~1044.7 eV and ~1021.6 eV were assigned to Zn $2p_{3/2}$ and Zn $2p_{1/2}$, further illustrating the enhanced lithiophilic characteristic by forming Zn–Li alloy (Fig. 1e).[46] N_2 adsorption/desorption measurements were then conducted to quantitatively assess the textural features of ZIF-8@RGO, ZIF-8@GO, and RGO materials. ZIF-8@RGO revealed a noticeably higher Brunauer–Emmett–Teller (BET) surface area of ~53.61 $m^2\ g^{-1}$ with a total pore volume of ~0.16 $cm^3\ g^{-1}$ than those of bare RGO (only 32.08 $m^2\ g^{-1}$/0.08 $cm^3\ g^{-1}$) and ZIF-8@GO (1215.4 $m^2\ g^{-1}$/0.91 $cm^3\ g^{-1}$), owing to the carbonization of ZIF-8 nanoparticles (Fig. 1f and S2†). Notably, the ultrahigh specific surface area and pore volume of ZIF-8@GO were attributed to the abundant ZIF-8 nanoparticles (seen in Fig. 1a); meanwhile, most ZIF-8 particles disappeared after high-temperature treatment, enabling the obvious reduced textural features of ZIF-8@RGO. Specifically, the inset pore size distributions manifested that more abundant and hierarchical pores ranging from 10 to 100 nm were formed in ZIF-8@RGO, as shown in Fig. 1g, allowing the facilitated access of electrolyte and promoted transfer of Li^+. And the connected pores provided spaces for Li metal accommodation and effectively buffered the huge volume change during Li plating/stripping. Raman spectroscopy was also conducted to evaluate the graphitization level, as shown in Fig. 1h and S3.† The identified peaks at around ~1340 cm^{-1} (corresponding to the vibration of disordered carbon atoms at the edge of graphite layer or a defective graphite structure) and ~1590 cm^{-1} (assigned to stretching vibration of C–C bond in sp^2 hybrid carbon atomic plane) were indexed to the D and G bands, respectively. Compared to GO and ZIF-8@GO materials, the slight reduction of I_G/I_D was attributed to partially repaired defects.[47,48] Nevertheless, the high value of I_G/I_D (~0.96) demonstrated the superior graphitization degree of ZIF-8@RGO, verifying the excellent electronic conductivity. Hence, it was expected that the porous and highly conductive 3D network with homogeneous nucleation sites in the free-standing ZIF-8@RGO scaffold would allow a reduced local current density during Li-plating/stripping, contributing to dendrite-free deposition, mitigated volume change and enhanced high capacity of Li utilization.

Li plating process on ZIF-8@RGO scaffold

To assess the lithiophilic property of as-prepared ZIF-8@RGO, dynamics evolutions and deposition behaviors with different areal capacities during lithium plating were explored by characterizing the nucleation overpotential and SEM morphology, respectively. The nucleation overpotential directly represents the energy barrier of Li nucleation and the lithiophilicity of the plating matrix. As expected, shown in Fig. 2a and S4a,† ZIF-8@RGO delivered a lowest nucleation overpotential of ~25 mV at a current density of 0.5 mA cm^{-2}, compared to bare Cu (~83 mV) and RGO (~30 mV), indicating the superior lithium plating kinetics of the ZIF-8@RGO architecture. Notably, ZIF-8@RGO also exhibited an only slightly increased

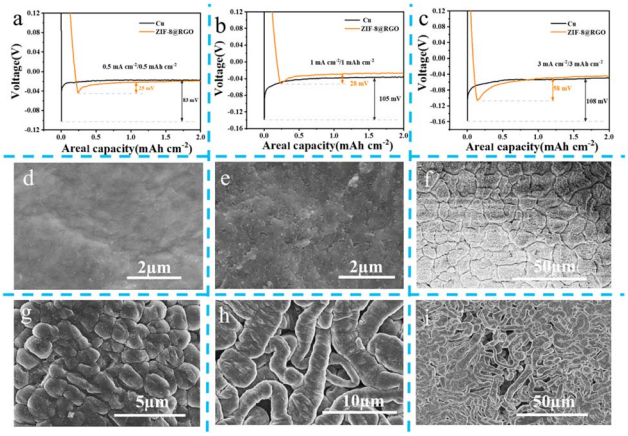

Fig. 2 Dynamics and morphology evolutions of lithium metal plating on bare Cu and ZIF-8@RGO. The discharge profiles of Li plating on Cu foil and ZIF-8@RGO (a–c), surface SEM morphologies of (d–f) ZIF-8@RGO and (g–i) bare Cu after plating (a, d and g) 0.5 mA cm^{-2}/0.5 mA h cm^{-2}, (b, e and h) 1 mA cm^{-2}/1 mA h cm^{-2}, (c, f and i) 3 mA cm^{-2}/3 mA h cm^{-2}.

nucleation overpotential of ~28 mV and ~58 mV at 1 mA cm^{-2}/1 mA h cm^{-2} and 3 mA cm^{-2}/3 mA h cm^{-2}, respectively. This suggested that the N/Zn seeding sites rendered the matrix of ZIF-8@RGO lithiophilic and minimized the nucleation barrier of lithium. In comparison, the other two cases presented unsatisfactory results for bare Cu (~105 mV/~108 mV for 1 mA cm^{-2}/3 mA cm^{-2}) and RGO (~41 mV/~65 mV for 1 mA cm^{-2}/3 mA cm^{-2}), depicted in Fig. 2b, c and S4b, c.† These behaviors were attributed to the synergistic effects of excellent conductivity capability and high specific surface area of RGO, as well as the existence of rich but homogenous N/Zn lithiophilic sites in the RGO matrix. Moreover, the lithiophilicity of ZIF-8@RGO was further demonstrated directly by the morphology evolutions over multiple plating capacities. After plating 0.5 mA h cm^{-2} Li, the surface of ZIF-8@RGO presented a smooth and flat appearance, indicating Li ions were predominantly deposited into the ZIF-8@RGO matrix. Intriguingly, smooth scaly lithium of about 0.5 μm in diameter and larger sized lumps being dendrite-free were also evenly distributed when plating was increasing to 1 mA h cm^{-2} and 3 mA h cm^{-2}, respectively (Fig. 2e and f). Hence, a high accommodation areal capacity with high utilization could be anticipated. Whereas, obvious tiny burr-like lithium dendrites were distributed on the RGO electrode with only ~1 mA h cm^{-2} Li plated on it (Fig. S4d†), suggesting the key role of N/Zn-rich seeding sites in the RGO matrix during plating. As the plating proceeds, severe Li agglomerations with a large number of cracks were deposited on the RGO due to uneven Li nucleation (Fig. S4e and f†). As for the bare Cu, lumps with different shapes and sizes were randomly distributed on the surface when plating 0.5 mA h cm^{-2} Li (Fig. 2g). Additionally, an obvious wormlike morphology of dendrites was observed after the plating capacity increased to 1 mA h cm^{-2}, which may induce the formation of uneven electrical field, accompanied with accelerated inhomogeneous Li plating.[49] Consequently, enlarged wormlike Li

forming a loose structure was covered on the bare Cu, accelerating the detrimental side reactions between Li metal and electrolytes, and finally resulting in lithium inventory loss and an electronically isolated network. Therefore, the improved dendrite-inhibition capability of ZIF-8@RGO hinged on the involvement of evenly distributed N/Zn lithiophilic sites into the RGO matrix. Furthermore, according to Sand's law,[26] the nucleation of dendrites in ZIF-8@RGO with high specific surface area was delayed due to the reduced local current density.

Reversible Li plating/stripping behavior with ZIF-8@RGO electrode

The cycling stability and voltage hysteresis of the Li/ZIF-8@RGO electrode were evaluated through galvanostatic cycling profiles. Specifically, the voltage hysteresis/overpotential presented a direct reflection of the voltage variation during plating/stripping. Li/ZIF-8@RGO electrode was fabricated by preloading 5 mA h cm^{-2} Li on the ZIF-8@RGO scaffold with galvanic deposition at a current density of 0.5 mA cm^{-2}. Similar electrochemical deposition methods were used to prepare Li/RGO and Li/Cu electrodes. The rate behavior of a symmetrical cell was first compared with three different electrodes, presented in Fig. 3a and S5.† Li/ZIF-8@RGO electrode demonstrated a stable charging voltage hysteresis of ~12, ~21, ~25, ~31, ~35 mV at a current density of 1, 2, 3, 4, and 5 mA cm^{-2}, respectively. However, larger voltage polarizations were presented for the other two cases, especially for the bare Cu electrode with ~131 mV at 5 mA cm^{-2}. Admittedly, the high specific kinetic obstacle in the bare Cu inclined to heterogeneous Li plating/stripping at larger rates.[50] Notably, the improved rate performance of ZIF-8@RGO indicated the enhanced kinetic process with homogeneous nucleation during plating/stripping, attributed to unimpeded 3D electron transport pathways and abundant lithiophilic N/Zn sites inside ZIF-8@RGO.

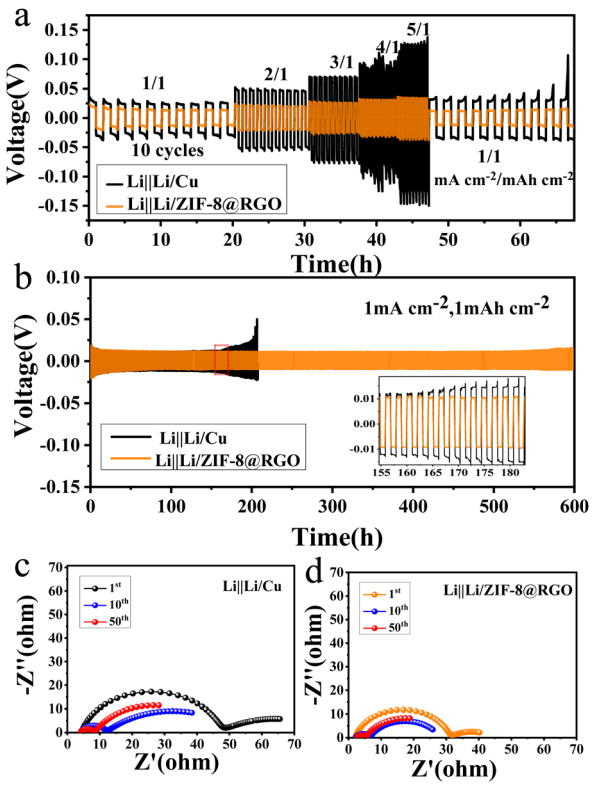

Fig. 3 Electrochemical performance evaluation of Li||Li half cells. Comparison of (a) the rate performance and (b) the cycling stability of Cu foil and ZIF-8@RGO in symmetric cells. Insets: magnified profiles during different periods. EIS spectra of (c) bare Cu and (d) ZIF-8@RGO for different cycles at 1 mA cm^{-2} for 1 mA h cm^{-2}.

Furthermore, the long-time cycling properties of three different symmetric collector cells at various current densities are exhibited in Fig. 3b, S6 and S7.† At a current density of 1 mA cm^{-2} with capacity of 1 mA h cm^{-2}, the symmetric cell with ZIF-8@RGO scaffold delivered a consistent hysteresis of ~10 mV with ultralong lifespans of over 600 h, while the other two symmetrical cells with RGO and bare Cu exhibited continually increased but fluctuating overpotential after 400 and 150 h, respectively (Fig. 3b and S6†). More impressively, the enhanced Li ion migration kinetics led to the significantly stable cycling performance of the ZIF-8@RGO cell with a lower voltage hysteresis of ~17 mV for more than 140 cycles even at a high current density of 2 mA cm^{-2}. In sharp contrast, the other two electrodes of RGO and bare Cu exhibited continuously increased voltage hysteresis with cycling lifespans of only 100 cycles and 60 cycles, respectively (Fig. S7†). Electrochemical impedance spectroscopy (EIS) measurements after various cycles were further performed to reveal the mechanism of significantly reduced polarization and very stable cycling with ZIF-8@RGO electrode during plating/stripping. As shown in Fig. 3c, d and S8a,† the bulk (R_s) and SEI interfacial resistance (R_{SEI}) were estimated from the semicircle at the high-frequency range. The corresponding equivalent circuit diagram is presented in the inset of Fig. S8a† and the simulated parameters are summarized in Fig. S8b–d.† It can be seen that the R_s and R_{SEI} values of the three electrodes gradually decreased upon cycling within 50 cycles, indicating a gradual stabilization process. Nevertheless, for the ZIF-8@RGO electrode, R_s and R_{SEI} exhibited always lower values compared to those of RGO and bare Cu, demonstrating a better electrode interface stability and much faster kinetic process originating from the enhanced lithiophilic properties and the benefits of the 3D high-conduction RGO scaffold.

The long-time cycling reversibility of the ZIF-8@RGO electrode was characterized by galvanostatic discharge/charge profiles, and RGO and Cu electrodes were also investigated for comparison. It can be seen that the coulombic efficiency of bare Cu electrode rapidly dropped to <~78% in the case of charging/discharging at 0.5 mA h cm^{-2} after 60 cycles (Fig. 4a), indicating the poorly reversible Li depositions of the bare Cu electrode. The corresponding voltage profiles of Li plating/stripping in Fig. 4b further demonstrated the poor reversibility of bare Cu, resulting from the unstable interface and disconnected electrical conduction paths by the repeated formation of dendritic Li. In contrast, the coulombic efficiency of the RGO electrode was ~98.61% over 200 cycles but then dropped to ~76.62% after 240 cycles (Fig. S9†). The relatively high coulombic efficiency in

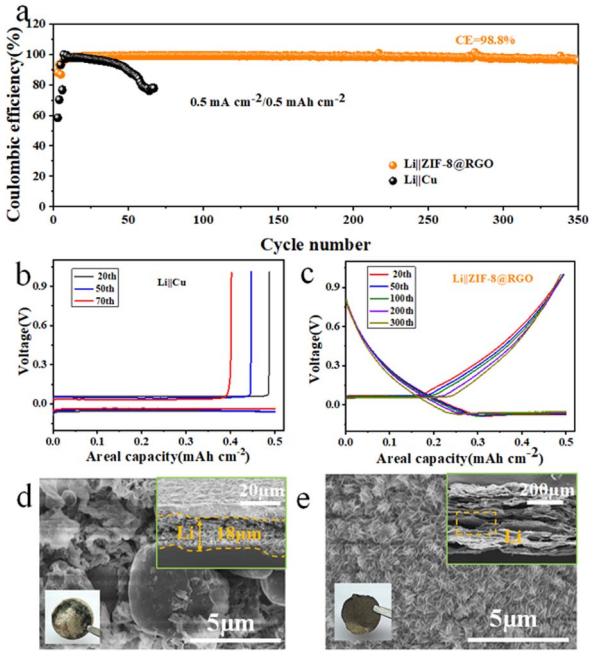

Fig. 4 Li metal plating/stripping behaviors on bare Cu and ZIF-8@RGO. (a) Coulombic efficiency comparison of bare Cu and ZIF-8@RGO, and the corresponding voltage profiles of Li plating/stripping on (b) bare Cu and (c) ZIF-8@RGO with a capacity of 0.5 mA h cm^{-2} at 0.5 mA cm^{-2}. SEM images of (d) bare Cu and (e) ZIF-8@RGO after 50 cycles at 0.5 mA cm^{-2} for 0.5 mA h cm^{-2}. Insets: corresponding cross-sectional and optical morphologies.

the case of RGO resulted from the mitigative effects on volume change of the 3D high-conduction RGO scaffold, in line with the results of corresponding voltage profiles during charging/discharging (Fig. S10†). Notably, the coulombic efficiency of the ZIF-8@RGO electrode was ~88.03% in the 1st cycle, and increased to ~95.03% and ~98.36% in the 2nd and 10th cycles, respectively. Moreover, the average coulombic efficiency of the ZIF-8@RGO electrode delivered a value of ~98.48% over 350 cycles. In addition, we designed an additional experiment to further evaluate the Li utilization of the anode. After preloading 1.5 mA h cm^{-2} at 0.5 mA cm^{-2} Li on ZIF-8@RGO, we investigated the potential hysteresis during long-term cycling in Li||ZIF-8@RGO. As shown in Fig. S11,† the symmetric cell with the ZIF-8@RGO scaffold delivered a consistent hysteresis of ~15.5 mV with long lifespans over 100 cycles, indicating the high utilization of 66.67% during the cycling. Specifically, the outstanding reversibility of ZIF-8@RGO benefited the high coulombic efficiency and superior cycling lifespan, which is verified in Fig. 4c.

To further demonstrate the regulating effect of ZIF-8@RGO on dendritic Li, the morphology variations (including both top and cross-section SEM images) of cycled metallic Li were recorded over 50 cycles at 0.5 mA cm^{-2} with a plating/stripping capacity of 0.5 mA h cm^{-2}. As depicted in Fig. 4d, a rough surface of bare Cu with excessive Li dendrites and dead Li and an additional thickness of ~18 μm were observed, indicating serious side reactions and uneven Li deposition. In addition, some island-like Li was nonuniformly covered on the RGO after 50 cycles (highlighted in Fig. S13a†). Meanwhile, the cross-sectional morphology revealed most Li (thickness of ~10 μm, Fig. S13b†) was distributed out of the RGO matrix, indicating only a partial amount of Li could reversibly insert into the 3D scaffold with lack of abundant N/Zn seeding sites. In contrast, the metallic luster of yellow with smooth surface in optical morphology of structure-integrity ZIF-8@RGO electrode (inset image in Fig. 4e) demonstrated the highly reversible plating/stripping behavior. Specifically, no obvious Li dendrites and thickness change were observed on ZIF-8@RGO electrode after 50 cycles, where most Li was embedded into the RGO matrix (Fig. 4e and S12†). Such completely different variation confirmed the synergetic merit of ZIF-8@RGO on inhibiting Li dendrites and alleviating dimension change from both aspects of the homogeneous lithiophilic nucleation sites and enhanced specific surface area.

Practical applicability of ZIF-8@RGO in full cells

The feasibility of the Li/ZIF-8@RGO electrode for practical deployments was further evaluated in full cells coupled with $LiFePO_4$ as cathodes. As shown in Fig. 5a and S15a,† the Li/ZIF-8@RGO||$LiFePO_4$ full cell presented a higher initial reversible specific capacity of ~143.0 mA h g^{-1} (corresponding mass energy density = 468.2 W h kg^{-1}) than those of Li/Cu@RGO||$LiFePO_4$ full cell (~138.8 mA h g^{-1}) and Li/RGO||$LiFePO_4$ full cell (~141.7 mA h g^{-1}) at 0.5C. Furthermore, compared to the other two cases, the Li/ZIF-8@RGO||$LiFePO_4$ full cell with limited Li in ZIF-8@RGO delivered a desirable cycling stability (capacity retention ratio of ~92.87%) with a highest discharge capacity of ~131.6 mA h g^{-1} even after 200 cycles. In sharp contrast, the Li/RGO electrode with lack of abundant N/Zn sites exhibited a fluctuating capacity after 130 cycles and a poor capacity retention ratio of ~52.92% over 200 cycles. Meanwhile, the capacity of Li/bare Cu||$LiFePO_4$ decreased to below 120 mA h g^{-1} with obvious fluctuations and

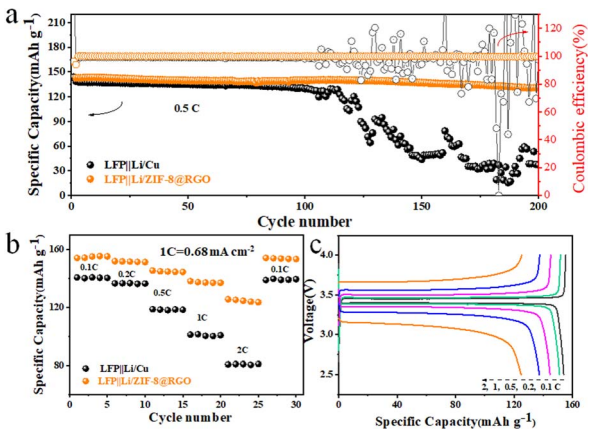

Fig. 5 Electrochemical performance evaluation in full cells. (a) Cycling performances. (b) Rate capabilities of full cells with two types of anodes at 0.5C coupled with $LiFePO_4$ cathode. (c) The corresponding charge–discharge profiles at different rates with Li/ZIF-8@RGO as anode.

then the cell rapidly failed after 100 cycles, indicating the continuous significant Li loss due to the growth of dendritic Li during charging/discharging. Notably, the Li/ZIF-8@RGO||$LiFePO_4$ full cell exhibited a significantly high capacity retention ratio up to ~97.83% for 100 cycles (as presented in Fig. S14a†). More impressively, the voltage polarization in the corresponding charging/discharging profiles (Fig.s S14a, b and S15b†) of Li/ZIF-8@RGO||$LiFePO_4$ was much more stable than those of the other two cell systems, verifying the significantly homogeneous Li plating/striping at interfaces. Performance comparisons of different anode electrodes coupled with $LiFePO_4$ cathodes are summarized in Table S2.† Besides, a better rate capability with Li/ZIF-8@RGO as anode in full cells could also be achieved compared with other cases especially at high rates. Specifically, as depicted in Fig. 5b and c, the Li/ZIF-8@RGO||$LiFePO_4$ cell delivered a superior discharge specific capacity of ~155.3, ~151.8, ~144.9, ~137.3, ~124.7 mA h g^{-1} at 0.1C, 0.2C, 0.5C, 1C, 2C, respectively. In addition, when the current came back to 0.1C, the cell still performed at its initial capacity, further demonstrating its promoted conduction and reaction kinetics. Nevertheless, when employing Li/RGO as anode, the full cell presented an inferior rate performance of ~153.7, ~149.6, ~142.1, ~133.4, ~120.2 mA h g^{-1} at 0.1C, 0.2C, 0.5C, 1C, 2C, respectively (Fig. S16†), suggesting the key role of enhanced lithiophilic properties. The encouraging cycling stability and rate capability of ZIF-8@RGO-based cells adequately confirmed the applicability of ZIF-8@RGO electrode for practical deployments in high-energy Li metal batteries.

Experimental section

Fabrication of ZIF-8@RGO

Preparation of ZIF-8@GO solution. The precursor GO (1 mg mL^{-1}) was fabricated by a standard modified Hummers' method. For synthesis of ZIF-8@GO, 0.366 g zinc nitrate hexahydrate (denoted as A solution) and 0.811 g dimethylimidazole (denoted as B solution) were first dissolved in 12 mL and 20 mL methanol solution, respectively. And then A solution was added to B solution to get a clear mixed solution. After that, 8 mL GO precursor (1 mg mL^{-1}) was immediately added into the above mixed solution, stirred at room temperature for 3 hours, followed by centrifuging with methanol (8000 rpm, 3 min) for 3 times, washed one time, and finally dispersed in deionized water before use. Notably, GO solution was pre-dispersed in methanol solution and ultrasonically dispersed for 5 hours (50%, 250 W).

Preparation of free-standing ZIF-8@RGO scaffold. ~6.78 mL of the above ZIF-8@GO solution (5.9 mg mL^{-1}) was mixed into ~200 mL of GO solution (2 mg mL^{-1}), and stirred at room temperature for 1 hour. Then, ~7.9 g ammonium bicarbonate was added into the solution. After stirring for 2 hours, free-standing ZIF-8@GO films (20 mL per sheet) were then filtered and followed by freeze-drying for 12 hours. Next, the freeze-dried ZIF-8@GO film was transferred to a porcelain boat and carbonized at 800 °C with nitrogen atmosphere for 3 hours with a heating rate of 5 °C min^{-1} to obtain free-standing ZIF-8@RGO film (thickness of ~300 μm). Finally, Li/ZIF-8@RGO electrode was prepared by electrodeposition. In the above preparation process, the corresponding Li/RGO electrode could be obtained without adding ZIF-8@GO precursors.

Material characterizations

The morphology and microstructure of materials were investigated with a field emission SEM instrument (S-4800 Hitachi). EDS (Oxford INCA) was carried out to obtain the elemental mapping results. Cycled Li/ZIF-8@RGO electrodes were investigated after 50 cycles, which were dissembled from cycled cells in an Ar-filled glove box and then gently rinsed with 1,2-dimethoxyethane (DME) to remove residual lithium salt. The nitrogen adsorption and desorption isotherms were measured *via* the BET method at 77.2 K with a Tri-star 3020 analyzer and the corresponding pore size distributions were calculated based on the Barrett–Joyner–Halenda model. Before testing, the samples were vacuum-degassed at 120 °C for 12 h. XRD patterns of materials were collected with a Rigaku D/MiniFlex 600/PC diffractometer using Cu Kα radiation (λ = 0.154 nm). The working voltage was 35 kV with a working current of 50 mA; the scanning range was 5–90° at 10° min^{-1}. Raman spectra were recorded with a DXR2 (Thermo Scientific) using 532 nm incident radiation. XPS measurements were carried out with an X-ray photoelectron spectrometer (Thermo Scientific ESCALAB Xi^+) using a monochromatic Al Kα X-ray source. XPS can be used to calculate the atomic composition and content (or relative concentration) of the sample surface, and give valence bond information and charge distribution of related elements. Notably, the samples were thoroughly dried before testing.

Electrochemical measurements

CR2032 coin cells were assembled in an Ar-filled glove box (H_2O/O_2 below 0.01 ppm) and tested with a Land 2001A battery testing system to evaluate the electrochemical performance. To measure the nucleating potential and coulombic efficiency, as-prepared ZIF-8@RGO, RGO, and bare Cu were employed as working electrode, metallic Li as the counter and reference electrode, 1 M lithium bis(trifluoromethanesulfonyl)imide (LiTFSI, DoDoChem, 99.8%) in 1,3-dioxolane (DOL, DoDoChem, 99.95%) and DME (DoDoChem, 99.95%) (volume ratio: 1 : 1) with 1% $LiNO_3$ (DoDoChem, 99.9%) was added as the electrolyte (a fixed amount of ~60 μL for each coin cell), and a Celgard 2400 membrane was used as the separator. The assembled asymmetrical Li/ZIF-8@RGO||Cu cells were first cycled at 0–1 V (*vs.* Li^+/Li) at 0.05 mA cm^{-2} for 3 cycles of activation. A certain amount of Li (~0.5 mA h cm^{-2}) was deposited on the working electrode and then stripped away up to 1 V (*vs.* Li^+/Li) for each cycle.

Furthermore, the developed symmetrical Li/ZIF-8@RGO, RGO, and bare Cu||Li metal cells were assembled by first pre-loading 5 mA h cm^{-2} of Li on the host and then charging/discharging at different current densities/capacities. The voltage polarization during the charge–discharge cycle was measured by fixing the charge–discharge current density/capacity to characterize the cycle stability and cycle life of the battery. EIS measurements were performed in cycled Li/ZIF-

8@RGO||Li cells using a CHENHUA electrochemical station in the frequency range of 10 mHz to 100 kHz with an amplitude of 5 mV. The interface transfer resistance of the battery and the performance of the SEI film were characterized by fitting data analysis of the impedance diagram.

Full cells were assembled with $LiFePO_4$ as the cathode, certain preloaded amount of Li as anode, and commercial ester electrolyte: 1.0 M phosphofluoric acid ($LiPF_6$, DoDoChem, 99.95%) in ethylene carbonate : diethyl carbonate (DoDoChem, 99.95%) = 1 : 1 vol% with 10.0% fluoroethylene carbonate (DoDoChem, 99.95%). The $LiFePO_4$ electrode was fabricated with fixed $LiFePO_4$, Super-P and polyvinylidene difluoride of 8 : 1 : 1 weight ratio in *N*-methyl-2-pyrrolidone (99.5%). The average area loading of the cathode was about 4 mg cm^{-2}. The as-prepared full cells were charged/discharged between 2.4 V and 4.0 V to assess the cycling stability and rate capability.

Conclusions

In summary, this work highlights a 3D lithiophilic ZIF-8@RGO free-standing scaffold for Li metal anodes. In particular, abundant N/Zn nucleation sites are *in situ* homogeneously embedded into the RGO skeleton by carbonized MOF ZIF-8 material, giving rise to significantly reversible dendrite-free Li^+ insertion/extraction into the RGO matrix during plating/stripping. Specifically, metallic Li is preferentially nucleated on those lithiophilic sites due to decreased local current density but outstanding 3D electronic conduction networks. Consequently, the synergetic merit of the ZIF-8@RGO structure enables lower overpotentials, enhanced Li transfer dynamics and alleviated changes in dimension, contributing to homogeneous Li deposition with promoted Li capacity utilization. As a result, the preloaded Li/ZIF-8@RGO electrodes deliver extraordinary rate capabilities and long-term cycling lifespans (>600 h) at a large specific capacity (5 mA h cm^{-2}) in symmetric cells and desirable coulombic efficiency of ~98.48% over 350 cycles. More impressively, full cells with limited Li coupled with $LiFePO_4$ cathode exhibit remarkable cycling stability and rate capability, further confirming the potential in practical applications. We believe the rational design principles of such 3D lithiophilic scaffolds will shed new light on addressing dendritic issues and high-capacity utilization for Li metal anodes.

Author contributions

Qi Liu: conceptualization, data curation, writing – review & editing. Rilei Wang & Zhenfang Liu: visualization, investigation, formal analysis, data curation. Cuiping Han: corrected and edited the manuscript. Xianshu Wang & Hongbo Liu: supervision, validation. Baohua Li: funding acquisition, supervision, validation, review & editing.

Conflicts of interest

There are no conflicts to declare.

Acknowledgements

This work was supported by Natural Youth Science Foundation of Hunan Province (no. 2022JJ40070), National Nature Science Foundation of China (no. 51872157 and no. 52072208), and Shenzhen Technical Plan Project (no. JCYJ20170817161753629). The authors thank the Materials and Devices Testing Center of Tsinghua University Shenzhen International Graduate School (Tsinghua SIGS).

Notes and references

1 M. Armand and J.-M. Tarascon, *Nature*, 2008, **451**, 652–657.
2 H. Kim, G. Jeong, Y. U. Kim, J. H. Kim, C. M. Park and H. J. Sohn, *Chem. Soc. Rev.*, 2013, **42**, 9011–9034.
3 W. Xu, J. Wang, F. Ding, X. Chen, E. Nasybulin, Y. Zhang and J.-G. Zhang, *Energy Environ. Sci.*, 2014, **7**, 513–537.
4 Q. Liu, Y. Wang, X. Yang, D. Zhou, X. Wang, P. Jaumaux, F. Kang, B. Li, X. Ji and G. Wang, *Chem*, 2021, **7**, 1993–2021.
5 Z. Yu, P. E. Rudnicki, Z. Zhang, Z. Huang, H. Celik, S. T. Oyakhire, Y. Chen, X. Kong, S. C. Kim, X. Xiao, H. Wang, Y. Zheng, G. A. Kamat, M. S. Kim, S. F. Bent, J. Qin, Y. Cui and Z. Bao, *Nat. Energy*, 2022, **7**, 94–106.
6 X. B. Cheng, R. Zhang, C. Z. Zhao and Q. Zhang, *Chem. Rev.*, 2017, **117**, 10403–10473.
7 D. T. Boyle, S. C. Kim, S. T. Oyakhire, R. A. Vila, Z. Huang, P. Sayavong, J. Qin, Z. Bao and Y. Cui, *J. Am. Chem. Soc.*, 2022, **144**, 20717–20725.
8 P. Shi, Z.-H. Fu, M.-Y. Zhou, X. Chen, N. Yao, L.-P. Hou, C.-Z. Zhao, B.-Q. Li, J.-Q. Huang, X.-Q. Zhang and Q. Zhang, *Sci. Adv.*, 2022, **8**, eabq3445–3455.
9 X. Fan, X. Ji, F. Han, J. Yue, J. Chen, L. Chen, T. Deng, J. Jiang and C. Wang, *Sci. Adv.*, 2018, **4**, eaau9245–eaau9255.
10 M. S. Park, S. B. Ma, D. J. Lee, D. Im, S. G. Doo and O. Yamamoto, *Sci. Rep.*, 2014, **4**, 3815–3822.
11 X. Fan, L. Chen, X. Ji, T. Deng, S. Hou, J. Chen, J. Zheng, F. Wang, J. Jiang, K. Xu and C. Wang, *Chem*, 2018, **4**, 174–185.
12 Q. Cheng, T. Jin, Y. Miao, Z. Liu, J. Borovilas, H. Zhang, S. Liu, S.-Y. Kim, R. Zhang, H. Wang, X. Chen, L.-Q. Chen, J. Li, W. Min and Y. Yang, *Joule*, 2022, **6**, 2372–2389.
13 Z. Wang, Y. Wang, B. Li, J. C. Bouwer, K. Davey, J. Lu and Z. Guo, *Angew. Chem., Int. Ed. Engl.*, 2022, **61**, e202206682–e202206692.
14 S. Xu, R. Xu, T. Yu, K. Chen, C. Sun, G. Hu, S. Bai, H.-M. Cheng, Z. Sun and F. Li, *Energy Environ. Sci.*, 2022, **15**, 3379–3387.
15 X. Peng, T. Wang, B. Liu, Y. Li and T. Zhao, *Energy Environ. Sci.*, 2022, **2022**, 1–12.
16 J. Su, M. Pasta, Z. Ning, X. Gao, P. G. Bruce and C. R. M. Grovenor, *Energy Environ. Sci.*, 2022, **15**, 3805–3814.
17 D. Yin, Z. Wang, Q. Li, H. Xue, Y. Cheng, L. Wang and G. Huang, *iScience*, 2020, **23**, 101869–101892.
18 S. Li, J. Huang, Y. Cui, S. Liu, Z. Chen, W. Huang, C. Li, R. Liu, R. Fu and D. Wu, *Nat. Nanotechnol.*, 2022, **17**, 613–621.

19 Y. Wang, Z. Wang, L. Zhao, Q. Fan, X. Zeng, S. Liu, W. K. Pang, Y. B. He and Z. Guo, *Adv. Mater.*, 2021, **33**, e2008133–e2008141.
20 H. Yuan, J. Nai, H. Tian, Z. Ju, W. Zhang, Y. Liu, X. Tao and X. W. D. Lou, *Sci. Adv.*, 2020, **6**, eaaz3112–eaaz3121.
21 M. Liu, S. Zhang, E. R. H. van Eck, C. Wang, S. Ganapathy and M. Wagemaker, *Nat. Nanotechnol.*, 2022, **17**, 959–967.
22 Q. Liu, D. Zhou, D. Shanmukaraj, P. Li, F. Kang, B. Li, M. Armand and G. Wang, *ACS Energy Lett.*, 2020, **5**, 1456–1464.
23 Q. Liu, Q. Yu, S. Li, S. Wang, L. Zhang, B. Cai, D. Zhou and B. Li, *Energy Storage Mater.*, 2020, **25**, 613–620.
24 P. Jaumaux, Q. Liu, D. Zhou, X. Xu, T. Wang, Y. Wang, F. Kang, B. Li and G. Wang, *Angew. Chem., Int. Ed. Engl.*, 2020, **59**, 9134–9142.
25 S. Jin, Z. Sun, Y. Guo, Z. Qi, C. Guo, X. Kong, Y. Zhu and H. Ji, *Adv. Mater.*, 2017, **29**, 1700783–1700789.
26 S. H. Wang, Y. X. Yin, T. T. Zuo, W. Dong, J. Y. Li, J. L. Shi, C. H. Zhang, N. W. Li, C. J. Li and Y. G. Guo, *Adv. Mater.*, 2017, **29**, 1703729–1703736.
27 S.-S. Chi, Y. Liu, W.-L. Song, L.-Z. Fan and Q. Zhang, *Adv. Funct. Mater.*, 2017, **27**, 1700348–1700358.
28 T. T. Zuo, X. W. Wu, C. P. Yang, Y. X. Yin, H. Ye, N. W. Li and Y. G. Guo, *Adv. Mater.*, 2017, **29**, 1700389–1700395.
29 J.-L. Yang, P. Yang, W. Yan, J.-W. Zhao and H. J. Fan, *Energy Storage Mater.*, 2022, **51**, 259–265.
30 C.-C. Wang, Y.-C. Lin, K.-F. Chiu, H.-J. Leu and T.-H. Ko, *ChemistrySelect*, 2017, **2**, 4419–4427.
31 F. Pei, A. Fu, W. Ye, J. Peng, X. Fang, M. S. Wang and N. Zheng, *ACS Nano*, 2019, **13**, 8337–8346.
32 M. Kim, X. Xu, R. Xin, J. Earnshaw, A. Ashok, J. Kim, T. Park, A. K. Nanjundan, W. A. El-Said, J. W. Yi, J. Na and Y. Yamauchi, *ACS Appl. Mater. Interfaces*, 2021, **13**, 52034–52043.
33 K. Lin, X. Xu, X. Qin, M. Liu, L. Zhao, Z. Yang, Q. Liu, Y. Ye, G. Chen, F. Kang and B. Li, *Nano-Micro Lett.*, 2022, **14**, 149–161.
34 K. Lin, X. Xu, X. Qin, S. Wang, C. Han, H. Geng, X. Li, F. Kang, G. Chen and B. Li, *Carbon*, 2021, **185**, 152–160.
35 H. Yuan, J. Nai, Y. Fang, G. Lu, X. Tao and X. W. D. Lou, *Angew. Chem., Int. Ed. Engl.*, 2020, **59**, 15839–15843.
36 G. Hou, X. Ren, X. Ma, L. Zhang, W. Zhai, Q. Ai, X. Xu, L. Zhang, P. Si, J. Feng, F. Ding and L. Ci, *J. Power Sources*, 2018, **386**, 77–84.
37 Z. Sun, S. Jin, H. Jin, Z. Du, Y. Zhu, A. Cao, H. Ji and L. J. Wan, *Adv. Mater.*, 2018, **30**, e1800884–e1800890.
38 Z. Zhou, N. Li, Y. Yang, H. Chen, S. Jiao, W.-L. Song and D. Fang, *Adv. Energy Mater.*, 2018, **8**, 1801439–1801448.
39 K. Lin, X. Qin, M. Liu, X. Xu, G. Liang, J. Wu, F. Kang, G. Chen and B. Li, *Adv. Funct. Mater.*, 2019, **29**, 1903229–1903340.
40 Q. Wang, T. Ina, W.-T. Chen, L. Shang, F. Sun, S. Wei, D. Sun-Waterhouse, S. G. Telfer, T. Zhang and G. I. N. Waterhouse, *Sci. Bull.*, 2020, **65**, 1743–1751.
41 Y. Xiao, S. Guo, Y. Ouyang, D. Li, X. Li, W. He, H. Deng, W. Gong, C. Tan, Q. Zeng, Q. Zhang and S. Huang, *ACS Nano*, 2021, **15**, 18363–18373.
42 Y. Yang, S. Q. Wang, H. Wen, T. Ye, J. Chen, C. P. Li and M. Du, *Angew. Chem., Int. Ed. Engl.*, 2019, **58**, 15362–15366.
43 W. Yao, J. Chen, Y. Wang, R. Fang, Z. Qin, X. Yang, L. Chen and Y. Li, *Angew. Chem., Int. Ed. Engl.*, 2021, **60**, 23729–23734.
44 A. Paul, G. Vyas, P. Paul and D. N. Srivastava, *ACS Appl. Nano Mater.*, 2018, **1**, 3600–3607.
45 D. S. Bin, Z. X. Chi, Y. Li, K. Zhang, X. Yang, Y. G. Sun, J. Y. Piao, A. M. Cao and L. J. Wan, *J. Am. Chem. Soc.*, 2017, **139**, 13492–13498.
46 K. Yan, Z. Lu, H.-W. Lee, F. Xiong, P.-C. Hsu, Y. Li, J. Zhao, S. Chu and Y. Cui, *Nat. Energy*, 2016, **1**, 1–8.
47 H. J. Shin, K. K. Kim, A. Benayad, S. M. Yoon, H. K. Park, I. S. Jung, M. H. Jin, H. K. Jeong, J. M. Kim, J. Y. Choi and Y. H. Lee, *Adv. Funct. Mater.*, 2009, **19**, 1987–1992.
48 S. Stankovich, D. A. Dikin, R. D. Piner, K. A. Kohlhaas, A. Kleinhammes, Y. Jia, Y. Wu, S. T. Nguyen and R. S. Ruoff, *Carbon*, 2007, **45**, 1558–1565.
49 D. Lu, Y. Shao, T. Lozano, W. D. Bennett, G. L. Graff, B. Polzin, J. Zhang, M. H. Engelhard, N. T. Saenz, W. A. Henderson, P. Bhattacharya, J. Liu and J. Xiao, *Adv. Energy Mater.*, 2015, **5**, 1400993–1401000.
50 N. W. Li, Y. X. Yin, J. Y. Li, C. H. Zhang and Y. G. Guo, *Adv. Sci.*, 2017, **4**, 1600400–1600406.